Materials and Design 164 (2019) 107548

Contents lists available at ScienceDirect

Materials and Design

journal homepage: www.elsevier.com/locate/matdes

Microstructural characterisation of Tristelle 5183 (Fe-21%Cr-10%Ni-7.5% Nb-5%Si-2%C in wt%) alloy powder produced by gas atomisation

M.J. Carrington [a,*], J. Daure [a], V.L. Ratia [a], P.H. Shipway [a], D.G. McCartney [a], D.A. Stewart [b]

[a] Advanced Materials Group, University of Nottingham, Nottingham NG7 2RD, UK
[b] Rolls-Royce plc, UK

HIGHLIGHTS

- Cooling rate significantly affects phase selection and microstructural formation in gas atomised Tristelle 5183.
- The solidification pathway of Tristelle 5183 notably changes with increasing cooling rate.
- The morphology of the carbonitride phase is influenced by cooling rate leading to micron- and nano-sized precipitates.
- Heavily undercooled powder particles are comprised of non-equilibrium microstructures and metastable phases.
- The clasification of as recieved Tristelle 5183 powder should be considered prior to hot isostatic pressing.

GRAPHICAL ABSTRACT

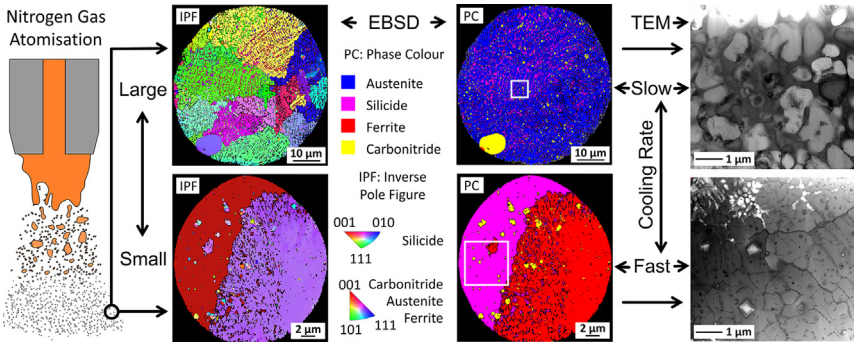

ARTICLE INFO

Article history:
Received 14 August 2018
Received in revised form 6 December 2018
Accepted 12 December 2018
Available online 14 December 2018

Keywords:
Metals and alloys
Coating materials
Nuclear reactor materials
Rapid-solidification
Quenching
Powder metallurgy
Precipitation

ABSTRACT

Nitrogen gas atomised powders of the hardfacing alloy Tristelle 5183 (Fe-21%Cr-10%Ni-7%Nb-5%Si-2%C in wt%) were sieved into different particle size ranges and their microstructures have been investigated. Powder particles larger than approximately 53 μm are composed of dendritic fcc γ-Fe as the principal phase with smaller quantities of: α-Fe, an interdendritic silicide phase isostructural to $Fe_5Ni_3Si_2$, and Nb(C,N). Particles <53 μm have increasing quantities of either dendritic α-Fe or cellular silicide phase with decreasing amounts of γ-Fe as the particle size decreases, along with ~5% Nb(C,N). Coarse (> 10 μm) sized Nb(C,N) particles, that are seen in all powder size fractions, pre-existed in the melt prior to atomisation, whereas micron-sized Nb(C,N) particles that are found within α-Fe, γ-Fe or silicide are the primary solidification phase. Nanoscale Nb(C,N) also formed interdendritically in the last stages of solidification. Compared with a mould cast sample, a significant difference is the suppression of M_7C_3 formation in all powder size ranges. The increasing quantities of α-Fe and silicide in smaller sized powder particles is consistent with increased undercooling prior to nucleation permitting metastable phase formation.

1. Introduction

Engineering components that are subject to wear, corrosion and/or oxidation are often given some form of surface engineering treatment to enhance their performance in aggressive environments. There are many techniques for applying protective coatings to a substrate and

* Corresponding author.
E-mail address: matthew.carrington@nottingham.ac.uk (M.J. Carrington).

https://doi.org/10.1016/j.matdes.2018.107548

weld hardfacing is one which is well established. Weld deposited hardfacings are commonly used when there is the possibility of significant wear and the need for long intervals between refurbishment. Cobalt-based weld hardfacing alloys are currently employed extensively and, more specifically, the Stellite™ family of alloys has found particularly widespread application because of their excellent performance in minimizing wear, corrosion and oxidation in many environments [1]. However, the use of cobalt-based hardfacing alloys is not always ideal. First, cobalt metal is a scarce commodity and is in increasing demand for use in batteries as well as many other fields [2]. Secondly, in nuclear applications, there is a need to reduce the cobalt content in alloys used to protect components in the primary circuit of a pressurized water reactor (PWR) power plant. When circulated through the reactor core, Co-based wear debris undergoes nuclear activation via neutron bombardment such that ^{59}Co is transmuted to the γ-emitting isotope ^{60}Co. The resulting ^{60}Co based radioactive debris has both a high and long-lived nuclear activity which is a hazard for maintenance personnel.

Consequently, significant efforts are being made to develop wear and corrosion resistant low-Co, iron-based alloys as described, for example, in references [3–8]. Alloys such as NOREM [9], Kennametal Stellite™ Tristelle 5183 [10–13] and more recently Nitromaxx [14] and RR2450 [6,13] have received significant attention. Traditionally, many of these hardfacing alloys have been designed for weld deposition with filler wire or plasma transferred arc (PTA) welding with the alloy in powder form. Tristelle 5183, which is the material of interest in the present paper, has the nominal composition Fe-21%Cr-10%Ni-7.5%Nb-5%Si-2%C (in wt%). It is reported to have good weldability and the weld deposited microstructure is described as comprising globular niobium carbide particles, a largely austenitic (fcc) dendritic iron-based matrix which is surrounded by an interdendritic, pearlitic-type eutectic containing a chromium carbide phase [10]. However, there is no clear understanding of how cooling rate affects microstructure formation. The corrosion and mechanical behaviour of Tristelle 5183 in comparison with Stellite 6 and other low cobalt alloys has been reported in, for example, references [3, 4, 9, 11, 13, 15, 16].

There are, however, disadvantages associated with the weld deposition of hardfacing layers. They inherently suffer from microstructural inhomogeneity, inclusions, porosity and weld metal dilution. Weld metal cracking, component distortion, heat affected zones within the substrate and residual stresses can also occur. Due to the safety critical nature and the long design lives required of the components used in nuclear applications, it is mandatory that the highest quality hardfacings are used. Therefore, interest has grown in producing hardfacing alloys by powder hot isostatic pressing (HIPing) [17]. Advantages of HIPing include better chemical and microstructural homogeneity and fewer defects [17]. Tristelle 5183 powder is manufactured by inert gas atomisation [18] and subsequently consolidated by HIPing at around 1100 to 1200 °C and ~100 MPa. HIP diffusion bonding is then used to join inserts, previously manufactured by HIP consolidation, to component substrates (typically 316 stainless steel) [19].

Whilst the importance of ensuring that Tristelle 5183 powder contains minimal undesirable inclusions is reviewed in reference [20], there is, to date, no work which investigates powder microstructure as a function of cooling rate, i.e. particle diameter. This topic is important because a wide powder particle size range, e.g. diameters below 500 μm, is typically employed in the powder HIPing process [21]. It is well known that gas atomized powder particles of different diameters cool at different rates, typically in the range 10^4 to 10^6 K/ s [18,22–24] However, it is currently not clear how cooling rate affects microstructure formation in the complex alloy under investigation in this study. At high cooling rates, different combinations of equilibrium and non-equilibrium phases may well form in powder particles of different sizes. This needs to be understood in order to properly select the powder size range used in HIP consolidation. A detailed investigation of the effect of cooling rate on microstructure formation in powder particles is crucial because a variation in the powder microstructure could affect the uniformity of the HIP consolidated product [25] and potentially give rise to undesirable property variations in a component.

The main aim of the present study was thus to investigate phase and microstructure formation in different size ranges of commercially available nitrogen gas atomized Tristelle 5183 powder in order to better understand phase selection during solidification by comparing the rapidly solidified microstructures with that of a conventionally cast alloy sample.

2. Materials and methods

2.1. Materials

The Tristelle 5183 powder used in this study was supplied by LSN Diffusion Ltd. (Ammanford, SA18 3GY, UK). The powder was manufactured using nitrogen gas atomisation to give a near-spherical powder particle morphology with a size range < 500 μm. A laboratory sieve shaker was used to separate the supplied powder into the following size fractions: <20, 20–38, 38–45, 45–53, 53–63, 63–75 and 75–106 μm, with characterisation of these different powder particle size ranges being undertaken in this work. The chemical composition of the powder reported in Table 1 was measured by inductively coupled plasma (ICP) spectrometry and Leco combustion analysis for the assessment of light elements namely, carbon and nitrogen. A conventionally cast sample of the alloy was obtained from the melt in the crucible just prior to gas atomisation. The alloy was poured from a ladle into a small hexagonal shaped ceramic shell mould to give a solidified sample ~ 30 × 30 × 12 mm^3 in size.

2.2. Materials characterisation

In order to perform microstructural analysis of the powder, sieved particles from different size ranges were mounted in conducting resin, ground, diamond polished to a 1 μm finish and then given a final polish using 0.06 μm colloidal silica. X-ray diffraction (XRD) analysis of powder in different size ranges was undertaken on unmounted particles. To examine the cast 5183 sample microstructure, a section was cut from around the mid-line of the sample, mounted in resin, ground and polished as described above.

Backscattered electron (BSE) imaging and electron backscatter diffraction (EBSD) analysis of samples were performed using a JEOL 7100F equipped with a field emission gun (FEG) and an Oxford Instruments Nordlys Nano EBSD detector. BSE imaging and EBSD were typically performed at an accelerating voltage of 15 kV. Oxford Instruments Aztec software was used to acquire EBSD data.

To examine powder samples in the transmission electron microscope (TEM), thin TEM lamellae were prepared using a focused ion beam (FIB) lift-out method. A FEI Scios DualBeam was employed for the initial preparation of site specific TEM lamellae whereby a standard lift out procedure was employed to achieve a sample thickness of ~150 nm. These lamellae required further thinning and cleaning for high resolution TEM (HRTEM). Both sides were thinned in a FEI Quanta 200 3D DualBeam employing Ga ions at an accelerating voltage of 10 kV and at an angle of ±2° to the sample surface to achieve a final sample thickness of ~100 nm. These additional FIB operations were performed diagonally across the sample surface and not in the direction of the original FIB operations.

A FEG source, FEI Talos F200X TEM operating at 200 kV was utilised for both scanning transmission electron microscopy (STEM) and elemental mapping via energy dispersive spectroscopy (EDS). The TEM-EDS mapping was performed using an FEI Super-X integrated EDS

Table 1
Composition of the Tristelle 5183 alloy as determined by chemical analysis.

	Fe	Cr	Ni	Nb	Si	C	N	Other
wt%	Bal.	21.72	10.39	6.90	4.67	2.08	0.05	0.73
at.%	Bal.	21.07	8.93	3.75	8.40	8.75	0.17	0.63

system. A JEOL 2100F FEG-TEM operating at 200 kV was employed for selected area diffraction (SAD) and high resolution transmission electron microscopy (HRTEM).

A Bragg-Brentano configured Bruker D500 X-ray diffractometer employing Cu–K_α radiation ($\lambda = 0.15418$ nm), equipped with a secondary beam graphite monochromator, was used for the identification of the phases present in the different powder size fractions. Scans were performed with a step size of 0.04° and a dwell time per step of 22 s in the 2θ range 20 to 120°. Rietveld refinements [26] were performed on XRD patterns using Topas V6 software in an effort to estimate phase fractions and to establish estimates for the refined lattice parameters. The so-called fundamental parameters approach to X-ray line profile fitting [27] was employed in the refinements presented in this study. The fundamental parameters approach is a convolution approach to line profile fitting whereby the final line profile can be built up from instrumental and sample aberrations which are convoluted with the emission profile.

3. Results

Powder particles in all size-ranges had a near-spherical external morphology, with evidence of attached satellites, consistent with manufacture by inert gas atomisation. The determination of the phases present and analysis of the microstructural features are described in the following sections.

3.1. Phase identification in the powder using XRD

Fig. 1 shows representative XRD patterns for the different powder size fractions normalised to the peak of maximum intensity on each diffractogram. All patterns show peaks which correspond to fcc γ-iron (austenite) at 2θ ~ 43.5°, 51° and 75°. Additionally, the patterns also have peaks at 2θ ~ 45°, 65° and 82.5°which index to bcc α-iron (ferrite). The relative intensities of both the bcc α-iron and fcc γ-iron reflections

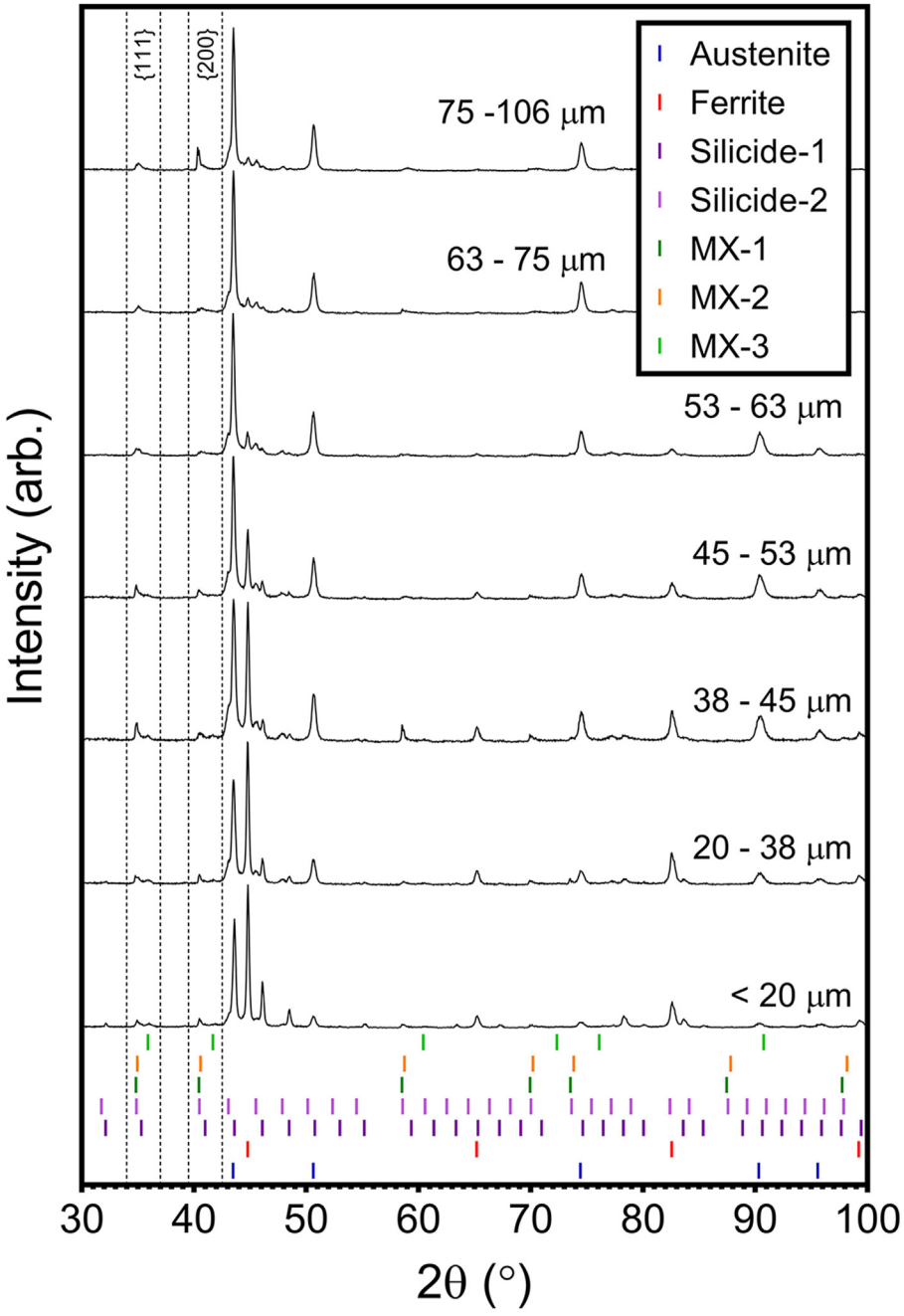

Fig. 1. XRD patterns obtained from the different powder size fractions of gas atomised Tristelle 5183. The vertical markers indicate the Bragg peak positions for the different phases.

Table 2
Comparison of measured and literature values for the lattice parameters of the silicide phases.

Sample	Phase	Lattice parameter (nm)
<20 μm powder	Silicide-1	0.6224
	Silicide-2	0.6298
63–75 μm powder	Silicide-1	0.6222
	Silicide-2	0.6302
Ackerbauer et al. [29]	$Fe_5Ni_3Si_2$	0.6146–0.6124
Gladyshevskii et al. [30]	$Cr_3Ni_5Si_2$	0.6120

are significantly dependent on the powder size fraction; the α-iron reflections exhibit a relative increase in intensity as the powder size decreases and the γ-iron reflections show a significant relative decrease in intensity with decreasing powder size.

All patterns show the presence of a B1 (Fm3m) NaCl-type, fcc MX carbonitride (M = metal atom, X = C,N) with a lattice parameter close to that of NbC [ICDD file #01-070-8416 for NbC]. The reflections consistent with this phase are clearly complex and can be interpreted as coming from three distinct populations of MX-type particles referred to as MX-1, MX-2 and MX-3. The evidence for these three distinct populations can be most clearly seen in the relatively low angle {111} (2θ ~ 34–37°) and {200} (2θ ~ 39.5–42.5°) reflections, which, for clarity have been marked on Fig. 1. The MX-3 population (at the higher 2θ values in the range of interest) has the smallest lattice parameter of the three MX populations and is consistent with the broad reflections that are most easily visible in the smaller powder size fractions. We interpret the remaining asymmetric reflections consistent with the MX carbonitride (at slightly lower 2θ values than the MX-3 peaks) as a convolution of reflections from the MX-1 and MX-2 populations. The asymmetry is a result of two effects: first, a population of particles, MX-2, that are compositionally non-uniform; and secondly, a population of particles, MX-1, that are microstructurally sparse and equilibriated, giving rise to peak height ratios that deviate from the ICDD database values for NbC. This analysis, based around an assumption of three populations, is justified by and entirely consistent with the microstructural observations on Nb(C,N) set out in Sections 3.2 and 3.3.

An additional two sets of reflections, consistent with an intermetallic silicide phase, are seen in all the diffraction patterns. This phase is cubic and isostructural to $Fe_5Ni_3Si_2$ and $Cr_3Ni_5Si_2$ [5,28,29]. These two sets of intermetallic silicide reflections are referred to as silicide-1 and silicide-2. The presence of two different sets of silicide reflections is most clearly illustrated by the two reflections situated at 2θ angles between 48° and 49°. The relative intensity of the silicide phase with the larger 2θ values (that designated silicide-1) clearly increases as the powder size decreases therefore, suggesting that this phase is present in a higher fraction in the smaller powder particles. The refined values of the lattice parameters of the silicide phases are reported in Table 2. The values differ significantly from the values reported in references [29, 30] but this is not surprising as in the present study the silicides formed under non-equilibrium conditions involving rapid growth from the melt whereas in previous studies solid state equilibrated systems were examined.

Overall, it is clear that there are broad similarities between the XRD patterns for 53–63, 63–75 and 75–106 μm powder size fractions. However, as the powder size decreases the diffraction patterns show more prominent α-Fe and silicide reflections. In light of the above, further analysis of XRD patterns was conducted on only two powder size fractions. These have been chosen as they are representative of the significant differences that are observed. The size fractions selected were the 63–75 μm size fraction (representative of the larger powder particles) and the <20 μm fraction (the smallest size range in the study). The Rietveld refinement method, employing a fundamental parameters approach, was applied to obtain quantitative estimates for phase fraction values as well as to determine refined lattice parameters. Fig. 2 shows

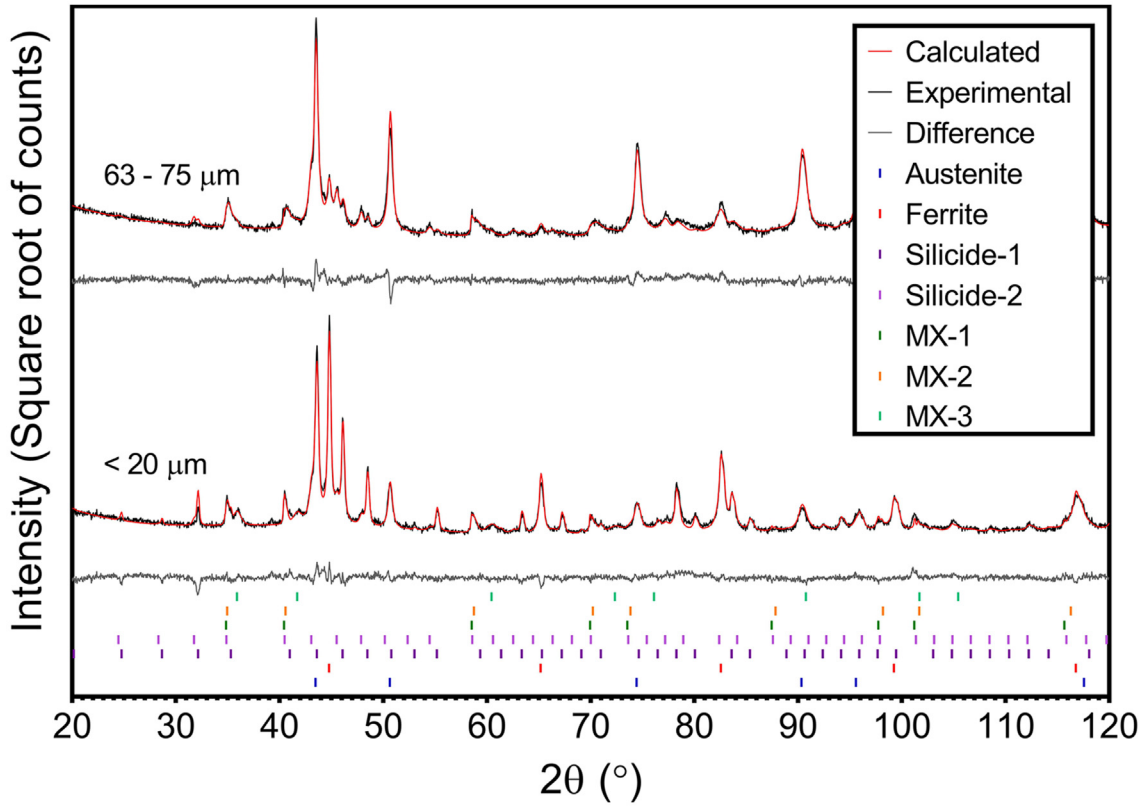

Fig. 2. Experimental XRD patterns (black) for the <20 μm and 63–75 μm powder size fractions. Calculated patterns determined via Rietveld refinement are indicated in red and the difference between experimental and calculated diffraction patterns is presented in grey. The vertical markers indicate the refined Bragg peak positions (based on the <20 μm powder fraction).

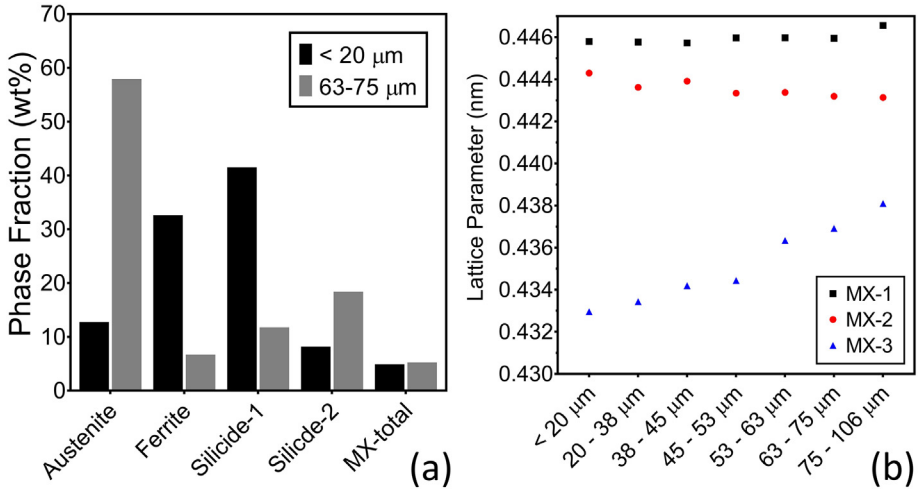

Fig. 3. (a) Depicts a bar chart showing the proportions of phases in the <20 μm and 63–75 μm powder size fractions from Rietveld refinements of XRD data. (b) shows a plot of refined lattice parameters for MX-1, MX-2 and MX-3 against powder size fraction obtained by Rietveld refinement.

full pattern fitting for these two powder size fractions; it is noted that the small difference between the calculated and experimental diffraction patterns illustrates that a sensible refinement has been achieved. The calculated phase fractions are reported in Fig. 3(a). The larger size powder comprises approximately 58% γ-Fe, 30% silicide, 7% α-Fe and 5% MX (in wt%) whereas the <20 μm powder fraction shows significantly different phase proportions with approximately 13% γ-Fe, 50% silicide 32% α-Fe and 5% MX (in wt%). Fig. 3(b) shows the refined lattice parameters of the MX-1, MX-2 and MX-3 populations in the different size fractions. It is apparent that the lattice parameter of the MX-1 and MX-2 populations changes very little with varying size fraction whereas that of MX-3 decreases as the powder size decreases. The refined value of the MX-1 population is close to the value 0.4469 nm given in the International Center for Diffraction Data file (#01-070-8416) for NbC suggesting that only this carbide formed under conditions close to stoichiometry.

In the section that follows, detailed microstructural observations are reported for the 63–75 μm and <20 μm powder size ranges to complement the detailed XRD analysis of these two size fractions.

3.2. Microstructure of 63–75 μm sized powder

Backscattered electron (BSE) images of a powder cross-section are shown in Fig. 4(a) and (b). The bright contrast features, which EDS showed to be a Nb-rich phase, are the MX populations identified by XRD. The single, large ~10 μm-sized Nb(C,N) particle in Fig. 4(a) will be termed a pre-existing carbide. From its size and rounded morphology, it seems probable that this large particle was present in the alloy melt prior to atomisation. The approximately micron-sized Nb(C,N) particles in Fig. 4(a) and (b) will be referred to as primary carbonitrides. These form a fine scale distribution of faceted crystals throughout the powder particle and are largely entrained within a dendritic network, Fig. 4(b). Nanoscale Nb(C,N) particles are also evident in the interdendritic regions (Fig. 4(b)) and will be termed secondary carbonitrides. The interdendritic phase region could not be definitively characterised by SEM-EDS but most likely corresponds to the silicide phase, isostructural to $Fe_5Ni_3Si_2$, detected by XRD.

Fig. 4(c) and (d) show an inverse pole figure (IPF) orientation map and a phase distribution map respectively, derived from EBSD analysis of a particle cross-section. A number of dendritic grains of γ-Fe are present which formed during the rapid solidification inherent in gas atomisation. A distribution of the micron-sized primary Nb(C,N) particles is also evident. The phase map (Fig. 4(d)) clearly shows that the interdendritic phase is a silicide isostructural with $Fe_5Ni_3Si_2$. The small fraction of material that could not be indexed is shown in black.

In order to gain further insight into the powder microstructure, STEM was performed on FIB lamellae prepared from the powder. The STEM bright field image, Fig. 5(a), shows dendritic features that are Ni-rich and Cr depleted compared to the interdendritic phase (Fig. 5 (b) and (c)). The dendrites are confirmed to be γ-Fe through the SADP in Fig. 5(d) (region marked (d) in Fig. 5(a)). The composition of a typical dendritic region, given in Table 3, shows significant Si in the γ-Fe. The SADP of Fig. 5(e) confirms that region marked (e) in Fig. 5(a) is a phase isostructural with $Fe_5Ni_3Si_2$ and the composition of typical silicide regions, also given in Table 3, shows that the Cr level is almost twice that of austenite. Finally, the EDS map of Fig. 5(f) confirms that the nanoscale interdendritic carbides, seen in the BSE image of Fig. 4(b), are indeed Nb rich. Both the primary and secondary Nb-based carbonitrides are distinctly visible in Fig. 5(a) and (f). An example of a primary particle which is entrained within the dendritic network is highlighted by the larger of the two white circles in Fig. 5(a) and (f). Similarly, a secondary carbonitride residing within the interdendritc region is highlighted by the smaller of the two white circles in Fig. 5(a) and (f).

3.3. Microstructure of <20 μm sized powder

Fig. 6(a) and (b) show an inverse pole figure (IPF) orientation map and a phase distribution map respectively derived from SEM/EBSD analysis of a powder particle cross section. The ferrite (α-Fe) and the silicide phases both occur as essentially single grains occupying approximately half the cross-section (Fig. 6(a)). The ferritic phase appears to conform to an irregular type dendritic morphology; this is particularly evident at the irregular dendritic front which separates the ferrite from the silicide, thus suggesting that the ferrite nucleated and grew first into the melt before its growth was terminated by impingement with the silicide phase. Micron-sized, Nb(C,N) particles are clearly distinguished in the phase map (Fig. 6(b)) and are dispersed in both the α-Fe and the $Fe_5Ni_3Si_2$ -type silicide phases.

To gain further insight into the microstructure, STEM and HRTEM were performed on a FIB lamella taken from a powder particle from the <20 μm size fraction. The bright field image, Fig. 7(a), reveals a predominantly cellular structure with a small dendritic region labelled b in the top left as well as faceted particles, one of which is labelled c. Fig. 7 (b) and (c) are the SADPs from regions labelled b and c respectively which confirm that these features are ferrite and fcc NaCl-type Nb(C, N) respectively. SADPs from the cellular-type matrix region, labelled d, and intercellular regions, such as e, both have the $Fe_5Ni_3Si_2$ silicide phase crystallography, despite showing different STEM contrast. The compositions of representative ferrite and cellular silicide regions, obtained by TEM-EDS, are given in Table 3. The two phases have similar

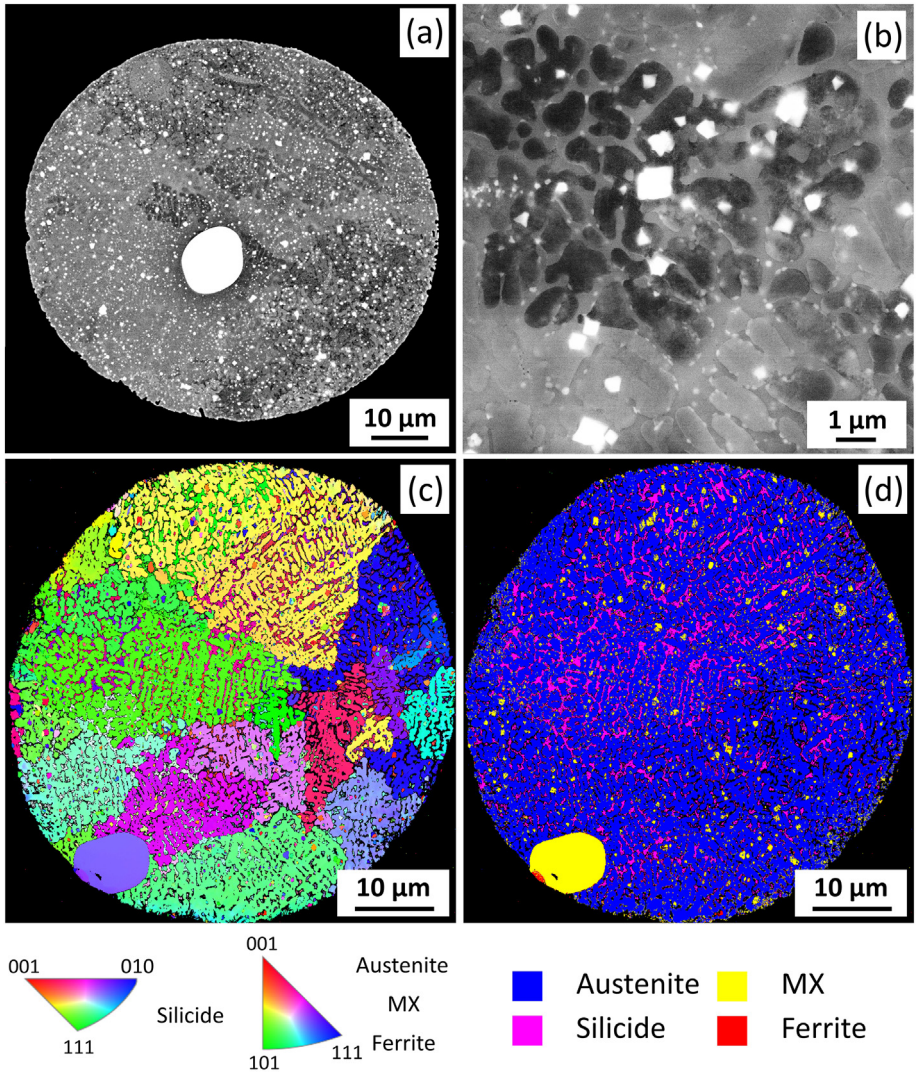

Fig. 4. (a) and (b) show SEM images of a cross section through powder particles consistent with the 63–75 μm powder size fraction. (a) is a low magnification BSE image showing a bright contrast rounded pre-existing Nb(C,N) particle and uniformly distributed primary Nb(C,N) particles. (b) is a high magnification BSE image showing the micron-sized primary Nb(C,N) particles within a dendritic matrix and secondary, nanoscale Nb(C,N) particles in the interdendritic regions. (c) and (d) respectively depict EBSD derived IPFZ orientation phase distribution maps. The colours of the grains in (c) correspond to the crystallographic axes in the relevant stereographic triangles, the corresponding phases can be identified in (d).

Si and Ni contents but there is a significantly higher Cr content in the silicide phase.

Fine nanoscale precipitates are seen to be almost entirely present at the intercellular boundary silicide regions (circled in Fig. 7(a)) and are shown in more detail in the STEM bright field image, Fig. 8(a). The EDS map for Nb, Fig. 8(b), reveals that they are Nb rich. The HRTEM image and corresponding FFT diffraction pattern, Fig. 8(c) and (d), confirm that they are nanoscale Nb(C,N) particles with, in the case of this precipitate, a lattice parameter ~0.42 nm.

3.4. Microstructural characterisation of cast Tristelle 5183

Fig. 9(a) shows an overlaid, EBSD-derived phase and band contrast distribution map of a representative section from the as-cast alloy. Fig. 9(b) shows an inverse pole figure (IPF) orientation map of the same section as Fig. 9(a). Fig. 9(c) and (d) are Nb and Si EDS maps of the same areas. Large scale (20–100 μm) Nb(C,N) particles are present, some of which show a dendritic morphology, whilst others are clusters of crystals with different orientations. These Nb(C,N) crystals are dispersed in a dendritic matrix which is austenite (γ-Fe), shown as the band contrast (light grey background) region of Fig. 9(a). Four phases occur in the last regions to solidify (interdendritic regions) which are: M_7C_3, bcc α-Fe (ferrite), and fine scale Nb(C,N) phase (Nb-rich and with a script morphology) and a silicide phase, based on the crystallography of $Fe_5Ni_3Si_2$. The silicide phase is generally found next to the α-Fe. The IPF map, Fig. 9(b) shows that the austenitic dendritic grain size is large, several hundred microns, consistent with slow cooling in conventional casting. The EDS map for Si (Fig. 9(d)) shows that it is preferentially segregated to the α-Fe and silicide regions. The proportions of the different phases in the cast structure, obtained from the EBSD data, are given in Table 4.

4. Discussion

4.1. Mould cast sample

This mould cast sample was obtained by pouring a small melt sample into a ceramic shell mould just prior to melt atomisation. To compare the cooling rate of the mould cast sample with that of the 63–75 μm powder fraction the secondary dendrite arm spacings of the γ-Fe

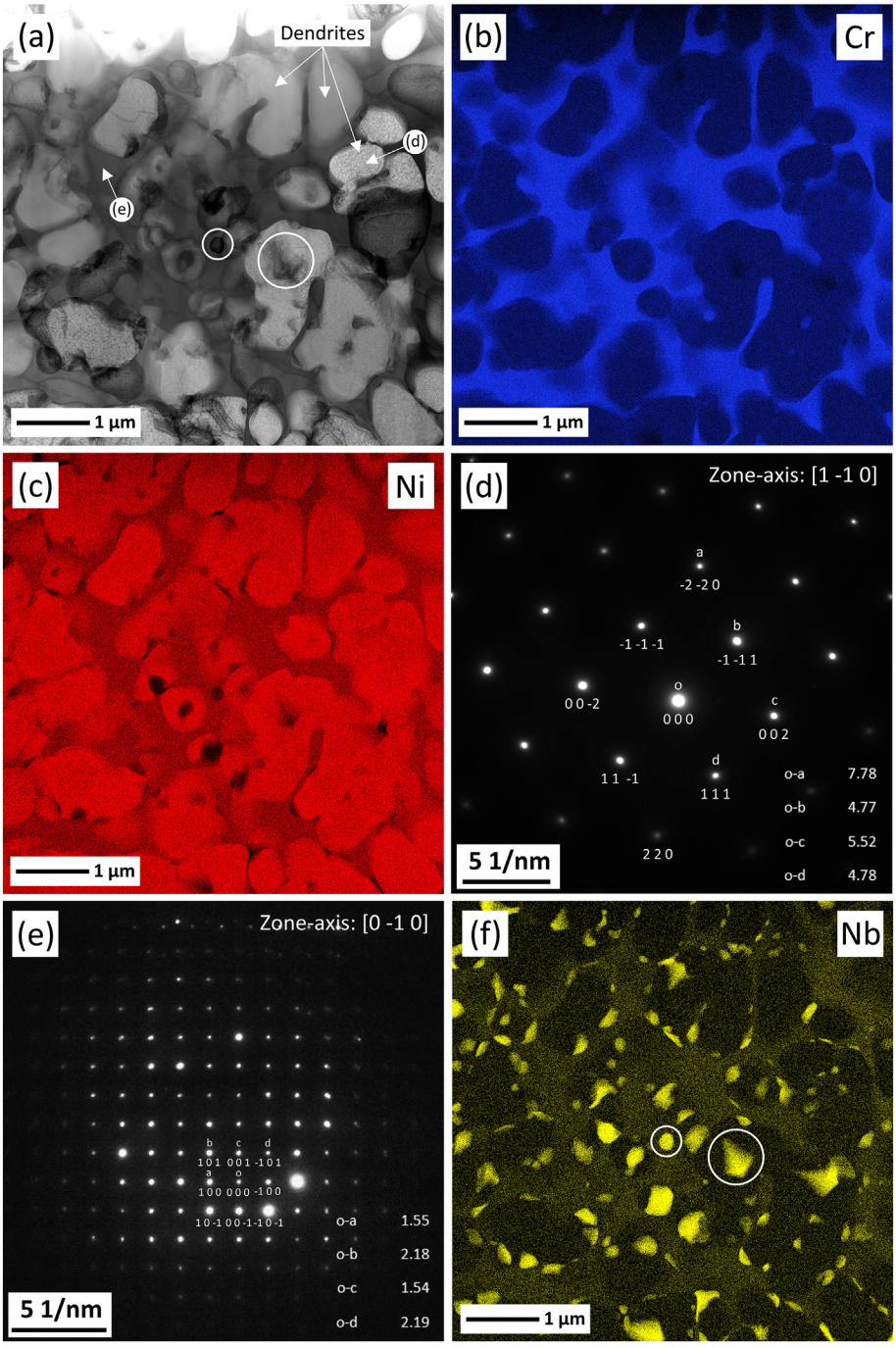

Fig. 5. Representative microstructure of a powder particle from the 63–75 μm size fraction. (a) is a bright field STEM image showing a dendritic matrix, an interdenritic phase as well as primary and secondary Nb(C,N) structures. (b), (c) and (f) show X-ray maps of the same region depicted in (a) and correspond to maps for Cr, Ni and Nb respectively. (d) and (e) show SAD patterns from the areas marked as e and d in (a). (d) shows an SADP indexed to fcc γ-Fe [1–10] zone axis and the pattern in (e) is indexed to a [0—10] zone axis of a phase isostructural to $Fe_5Ni_3Si_2$. (f) clearly shows the locations of the Nb-rich particles.

Table 3
Compositions in at.% (excluding carbon) of phases present in gas atomised powder from different size ranges obtained by EDS in the TEM.

Powder size range	Phase	Element (at.%)				
		Fe	Cr	Ni	Si	Nb
<20 μm	α-Fe dendrites	60.8 ± 0.3	15.3 ± 0.2	11.2 ± 0.3	10.1 ± 0.2	0.2 ± 0.1
	Cellular Silicide	54.3 ± 0.1	22.0 ± 0.1	9.7 ± 0.1	10.6 ± 0.1	1.0 ± 0.1
63–75 μm	γ-Fe dendrites	59.2 ± 0.6	17.1 ± 0.2	10.6 ± 0.2	10.5 ± 0.4	0.3 ± 0.1
	Interdendritic silicide	43.7 ± 0.3	33.4 ± 0.5	7.1 ± 0.1	11.0 ± 0.3	1.9 ± 0.1

Table 4
Proportions of phases in cast Tristelle 5183 from EBSD-derived data (unindexed indicates fraction of analysed area which could not be assigned to a phase).

Phase	γ-Fe	Cr_7C_3	Nb(C,N)	α-Fe	Silicide	Unindexed
Vol%	76	10	7	4	2	1

dendrites were measured. Using Eq. (1) below, that relates secondary dendrite arm spacing, λ_s, to cooling rate, $\frac{dT}{dt}$, where K is a constant for the alloy [31]:

$$\lambda_s = K\left(\frac{dT}{dt}\right)^{-0.33} \quad (1)$$

It is found that the cooling rate of the mould cast sample is ~10^{-5} times that of the 63–75 μm powder, i.e. around 0.8 K/s. By careful interpretation of the cast microstructure, the following solidification sequence can be proposed for Tristelle 5183 alloy under slow cooling conditions:

$$Liquid \rightarrow Liquid + Nb(C,N) \rightarrow Liquid + Nb(C,N) + Fe(\gamma) \rightarrow Liquid + Nb(C,N) + Fe(\gamma) + M_7C_3 + Nb(C,N)_{(script)} \rightarrow Nb(C,N) + Fe(\gamma) + M_7C_3 + Nb(C,N)_{(script)} + Fe(\alpha) + Fe_5Ni_3Si_2$$

The above sequence implies that the alloy can be regarded as hypereutectic and that the Nb(C,N) phase is the first to solidify (primary phase) with a faceted or, in some cases, dendritic morphology. These coarse Nb(C,N) particles are in some cases up to 100 μm in size and some agglomerates are seen. This could be because the alloy charge in the atomisation crucible was below the liquidus temperature (i.e. in the L + Nb(C,N) phase field) when the sample was taken for casting. In order to assess the feasibility of this interpretation, the liquidus temperature of Tristelle 5183 was calculated using ThermoCalc [32] and the TCFe7 steels database. The liquidus temperature of the alloy, i.e. the temperature for the reaction L → L+ Nb(C,N), is found to be ~1700 °C. This is above the probable processing temperature of the melt in the crucible and therefore supports the hypothesis that some large carbides pre-existed in the alloy charge prior to gas atomisation and could well have agglomerated during the holding time.

Under the slow cooling conditions of mould casting it is evident that solidification continues with the nucleation and growth of dendritic γ-Fe phase. From the EBSD inverse pole figure (IPF) map, Fig. 9(b), it is evident that the γ-Fe grain size is large, i.e. there are relatively few nucleation events, suggesting that Nb(C,N) particles do not act as potent nucleation sites for the γ-Fe phase. However, the coarse Nb(C,N) particles are not apparently pushed by the solidifying dendrites into interdendritic regions but instead the γ-Fe dendrites engulf the Nb(C,N) as they grow.

It is apparent from the microstructure that the M_7C_3 phase is the next significant phase to precipitate out on continued cooling as it is located in the interdendritic regions and has a volume fraction (Table 4) of almost 10 vol%. Other phases which are observed in the latter regions to solidify are Nb(C,N) (with a Chinese script-shaped morphology), α-Fe and a silicide phase isostructural with $Fe_5Ni_3Si_2$ but whose precise composition is uncertain. The morphology of the interdendritic Nb(C,N) clearly indicates that it formed by solidification. However, it is currently unclear whether α-Fe and $Fe_5Ni_3Si_2$ both form by solidification or whether α-Fe forms from the melt and $Fe_5Ni_3Si_2$ forms subsequently by a solid state transformation at a lower temperature.

4.2. Phase selection and microstructure formation in powder particles

4.2.1. Cooling rate considerations

As described by Yule and Dunkley [18], the cooling rate, $\frac{dT_d}{dt}$, of a liquid droplet in the gas atomisation process, prior to the onset of solidification, can be estimated from the well-known heat flow equations as follows, providing a number of simplifying assumptions are made as discussed in Supplementary data:

$$\frac{dT_d}{dt} = -\left(\frac{6h}{D\rho_d c_{p_d}}\right)(T_d - T_g) \quad (2)$$

where h is the heat transfer coefficient between the droplet and the atomising gas (h is a function of the dimensionless Nusselt number), T_d is the droplet temperature, T_g is the gas temperature, D is the droplet diameter, ρ_d is the density of the droplet and c_{p_d} is the specific heat of

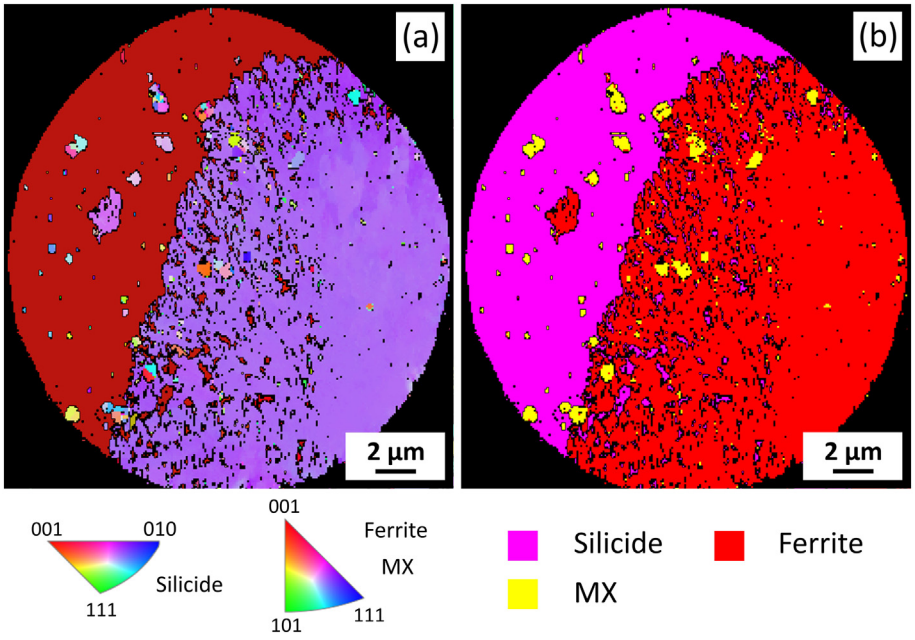

Fig. 6. (a) and (b) respectively show EBSD derived IPFX orientation and phase distribution maps of a powder cross section consistent with the <20 μm powder size fraction. The colours of the grains in (a) correspond to the crystallographic axes in the relevant stereographic triangles, the corresponding phases can be identified in (b).

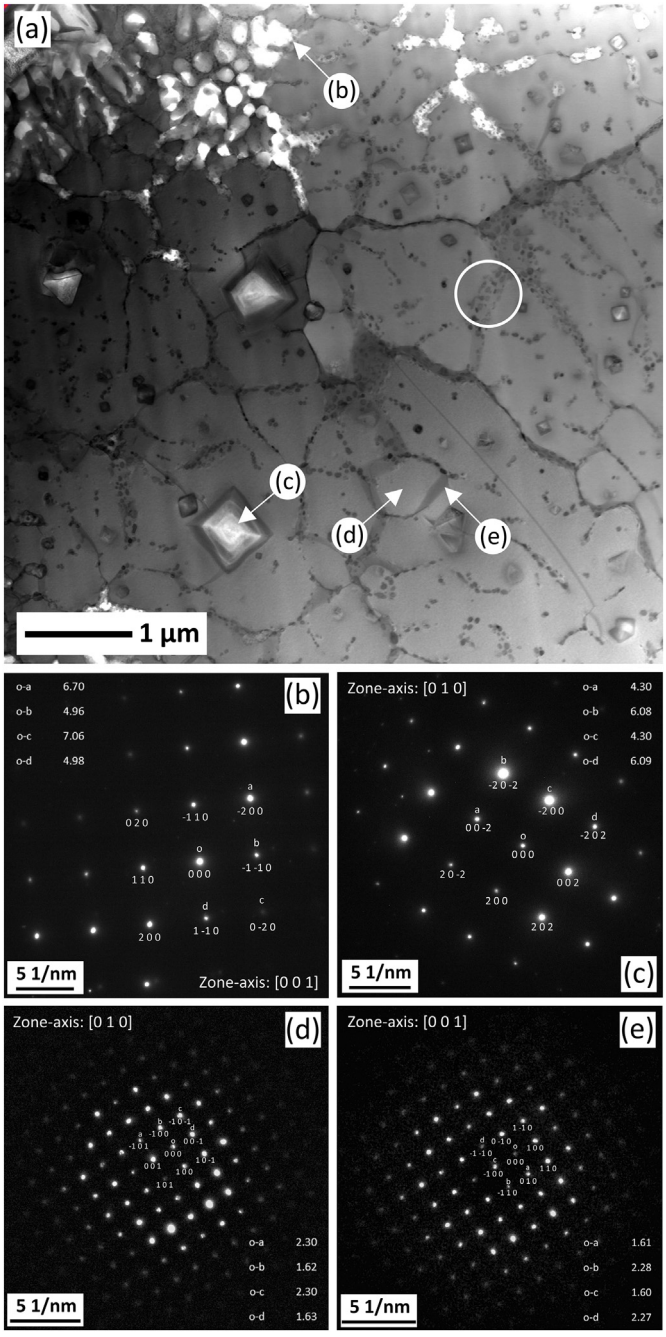

Fig. 7. Representative microstructure of a powder particle from the <20 μm size fraction. (a) depicts an STEM bright field image where the regions marked (a), (b), (c) and (d) correspond to the respective SADP's. (a) shows a dendritic region (b), an angular particle (c), a matrix phase with a cellular structure (d) and a cellular boundary region (e). (b) is indexed to α-Fe [001], (c) is Nb(C,N) [010], (d) and (e) exhibit the zone axes [010] and [001] of a phase isostructural to $Fe_5Ni_3Si_2$.

the liquid droplet (J kg^{-1} K^{-1}). Details of the assumptions and thermophysical parameters employed for nitrogen gas-atomised Tristelle 5183 are given in Supplementary Data. The calculations set out in the Supplementary Data reveal that the cooling rate of a 20 μm droplet is ~7×10^5 K/s and that of a 75 μm droplet is ~8×10^4 K/s assuming relative gas velocity of 40 m/s. However, the dominating factor is droplet diameter and clearly the two size fractions examined in detail in this work (<20 μm and 63–75 μm) have cooling rates that differ by approximately an order of magnitude, with this difference being relatively insensitive to other assumptions including that of relative gas velocity and gas temperature.

4.3. MX formation

It is evident from the XRD patterns, Fig. 1, that the MX phase is present in all powder size fractions. Furthermore, the detailed microstructural examination of powder cross-sections from the <20 and 63–75 μm size fractions confirmed the presence of Nb(C,N) particles of significantly different sizes. This is strong evidence that the MX populations identified by XRD correlate directly with the Nb(C,N) particles identified by microscopy and EDX analysis.

In, for example, the 63–75 μm powder fraction, large pre-existing Nb(C,N) particles are clearly observed in a number of particle cross sections (Fig. 4(a) and (d)). The size and, in some cases, rounded morphology of such particles strongly suggests that they did not form during the rapid solidification conditions imposed by gas atomisation. It seems more likely that they were present in the melt prior to gas atomisation as explained in Section 4.1 for the mould cast sample. Subsequently, we refer to these particles as pre-existing Nb(C,N). These pre-existing particles can be seen in all the powder size fractions but are more frequently observed in the larger powder size fractions. This further supports the hypothesis that large Nb(C,N) pre-existed in the alloy charge prior to atomisation as, during atomisation, there is a greater statistical likelihood of small powder particles being free from large Nb(C,N)particles.

Finer scale (both micron and nano-scale) Nb(C,N) particles are also evident in all the powder particles investigated through electron microscopy. It seems most likely that these nucleated from the melt and remained small due to the limited time available for growth during the atomisation process. A more detailed interepretation of the formation of these fine scale carbides, termed primary and secondary Nb(C,N) is discussed below.

XRD (Fig. 1) has allowed the identification of three different MX-type carbonitride populations, all of which are crystallographically consistent with Nb(C,N). We now argue that the MX populations are related to the three Nb(C,N) particle populations observed by SEM/TEM in the powder, namely (i) the pre-existing Nb(C,N); (ii) the micron-sized primary Nb(C,N) and (iii) the nano-scale secondary Nb(C,N). The sharp peak shapes and preferred orientation associated with the MX-1 population are indicative of a carbonitride that is both equilibrated and microstructurally sparse. The MX-1 population exhibits a lattice parameter of ~0.446 nm that is close to the value of 0.447 nm reported by Storms et al. [37] for stoichiometric NbC. Therefore, the XRD peak contributions identified as MX-1 are most likely to result from the pre-existing Nb(C,N) population that formed under near equilibrium conditions. The broad and somewhat asymmetric nature of the XRD peaks identified as MX-2 are characteristic of a population that has precipitated out and grown during solidification; it is expected that both the composition and lattice parameter increasingly deviate away from equilibrium due to compositional segregation effects during growth. The MX-2 population has an averaged approximate lattice parameter of ~0.444 nm which, in accord with the work of Storms et al. [37], is typical of a niobium carbide which has formed under conditions which notably deviate from equilibrium. In light of the above, the MX-2 population is attributed to the primary micron-sized Nb(C,N) (identified through electron microscopy) that precipitated directly from the melt prior to iron-matrix phase nucleation. The lattice parameter of the MX-3 population decreases with increasing cooling rate and is significantly smaller than those of the other two MX populations; notably, it decreases from ~0.438 to ~0.432 nm as the powder size decreases i.e. as the cooling rate increases. The increasing deviation from the equilibrium value would indicate that this MX-3 population formed far from equilibrium during droplet solidification and crystals are carbon deficient with respect to the stoichiometric NbC formula [33]. The sensitivity to cooling rate and high deviation

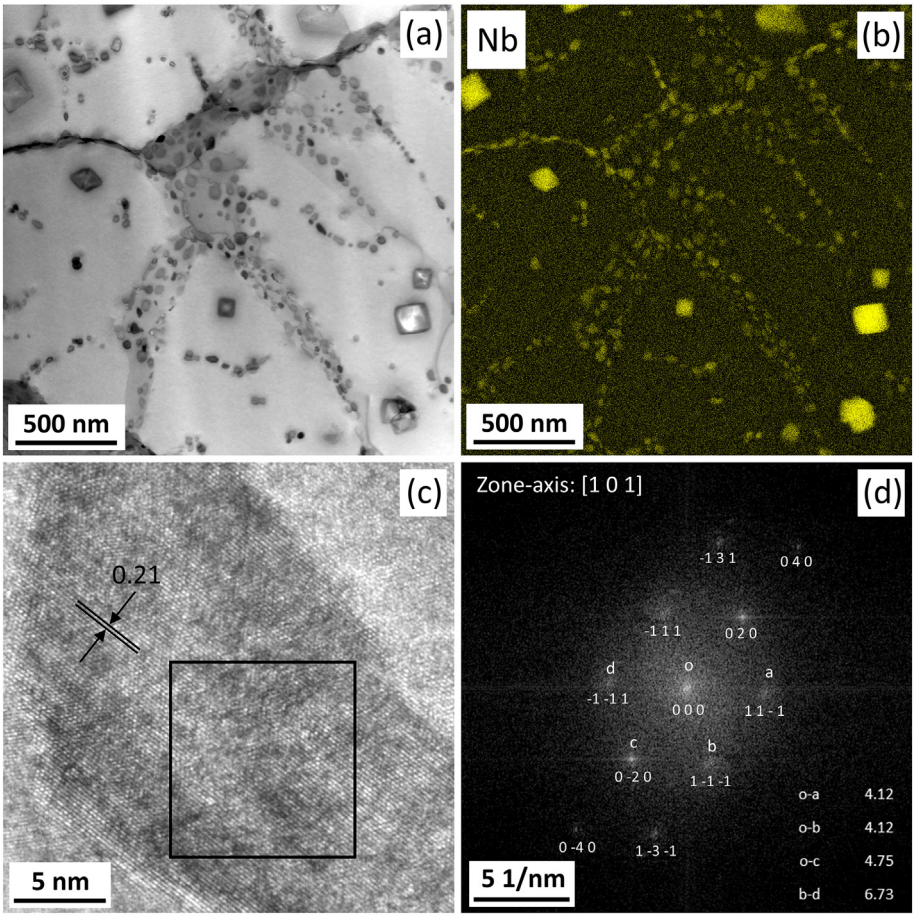

Fig. 8. Microstructure of the intercellular region of a particle consistent with the <20 μm size fraction. (a) illustrates a STEM bright field image which shows nanoscale particles in the silicide matrix. (b) illustrates a Nb EDS map of the region depicted in (a). (c) shows a HRTEM micrograph of a Nb-rich precipitate and (d) shows the corresponding FFT diffraction pattern from the box region depicted in (c), indexed to Nb(C,N) [101] zone axis.

from equilibrium could suggest that the MX-3 population is consistent with the nano-scale Nb(C,N) particles which precipitate out in the very last stages of solidification.

4.4. Effect of powder particle size on solidification behaviour

The solidification path taken by Tristelle 5183 is clearly different for different powder size fractions as has been revealed by the variation in the XRD patterns presented in Fig. 1 and further supported by the more detailed microstructural examination of the <20 and 63–75 μm powder size fractions. There are two important phenomena to consider before discussing the detail of microstructural evolution. First, there is the well-known increase in cooling rate during gas atomisation with decreasing droplet diameter [18,22]. Secondly, the sub-division of the melt during atomisation leads to finer droplets being less likely to contain potent heterogenous nuclei. The combined effect is that finer droplets are more likely to achieve larger undercoolings before solid phase nucleation occurs and so are more likely to solidify directly to metastable phases rather than forming equilibrium phases on cooling.

It is apparent from Fig. 1 that powder size fractions of 53–63 μm and above form predominantly γ-Fe with smaller amounts of MX, α-Fe and silicide phases. It is evident that the solidification pathway is markedly different from that of the mould cast sample as M_7C_3 formation has been wholly suppressed. Under the constraint of either slow nucleation or growth kinetics, stable phases may be suppressed at higher cooling rates and metastable equilibria may develop [34]. The suppression of M_7C_3 is believed to be due to its slow nucleation and growth kinetics as it has a complex crystal structure. Additionally, the dendrite arm spacing is significantly refined compared to the mould cast sample with an average value ~0.7 μm (Fig. 4(c–d)) compared with ~18 μm (Fig. 9) in the mould cast sample. It is also notable that in Fig. 4 a clear distinction between pre-existing Nb(C,N) (up to 20 μm) and primary Nb(C,N) (micron sized) can be seen, with the latter presumably nucleating from the melt during cooling. Fig. 4(b) shows the entrainment of primary Nb(C,N) within the γ-Fe dendrites due to the high initial growth rate of the latter immediately following nucleation. Solute elements Cr, Nb, Si and C are all rejected from the γ-phase dendrites during solidification into the interdendritic liquid which must then solidify in the post-recalescence stage of droplet cooling [22]. This leads to the formation of the nanoscale interdendritic particles seen in Fig. 4(b) and which TEM (Fig. 5) shows to be Nb(C,N) and which we refer to as secondary Nb(C,N). These particles are surrounded by an additional (distinct) interdendritic phase which has the crystallography of $Fe_5Ni_3Si_2$ but which contains significant Cr. This interdendritic silicide phase is seen to be significantly Cr-enriched compared with the γ-Fe dendrites and this can be attributed to the Cr rejection from the γ-phase dendrites.

In the case of powder size fractions below the 45–53 μm range, it is clear from Fig. 1 that increasing quantities of bcc α-Fe and silicide phase form with decreasing powder particle size range. This is confirmed by the quantitative Rietveld analysis data shown in Fig. 3. In general, it is through that the deep undercooling of the liquid during atomisation makes it possible to access the formation of one or more metastable phases [34–36], this is clearly possible in this alloy system for sufficiently high cooling rates of droplets. The formation of α-Fe

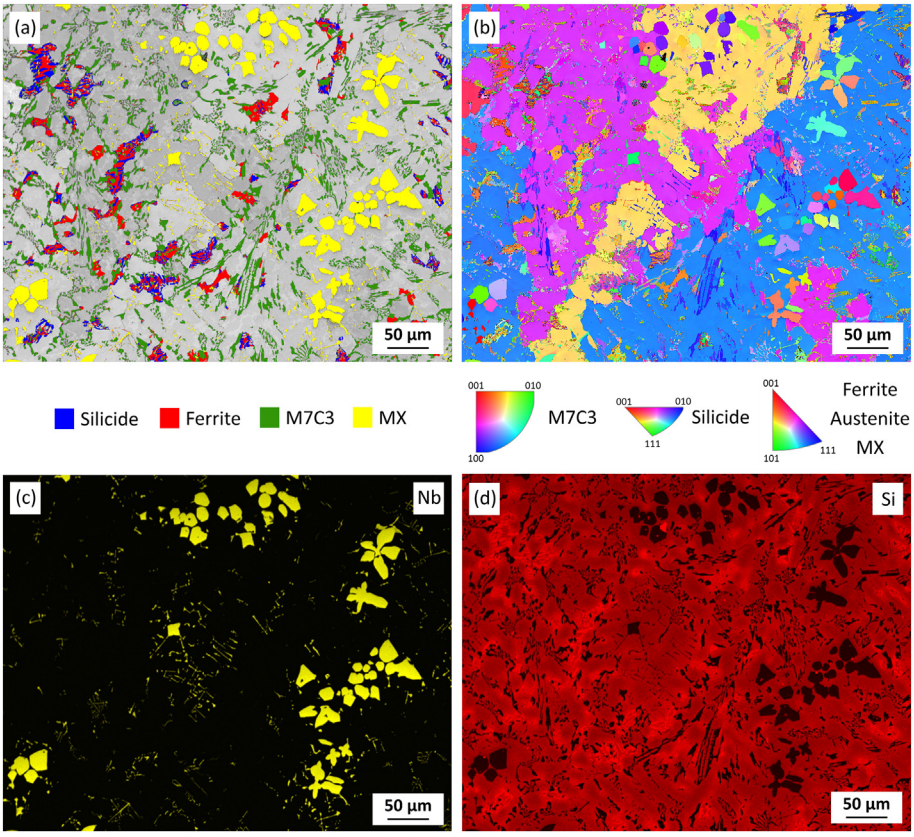

Fig. 9. Typical microstructure of cast Tristelle 5183 alloy. (a) Shows a phase distribution map overlaid onto a band contrast map derived from ESBD data showing large Nb(C,N) crystals in a γ-Fe dendritic matrix (grey) with interdendritic Cr_7C_3, Nb(C,N), bcc α-Fe and a phase isostructural to $Fe_5Ni_3Si_2$. (b) shows a IPFY orientation map, where the colours of the grains correspond to the crystallographic axes in the stereographic triangle for each phase. (c) and (d) are EDS maps of Nb and Si respectively confirming that the large crystals are Nb-rich and that Si is preferentially segregated to the interdenritic α-Fe and silicide phases.

directly from the melt in the present alloy is consistent with previous work involving fine powder particles of binary or ternary austenitic iron-based alloys which were gas atomised and rapidly cooled [37,38]. Both of these groups have reported the formation of bcc or α-Fe as the crystallization phase in the smaller powder (more rapidly cooled) particles whilst fcc or γ-Fe was the crystallization phase in larger diameter (more slowly cooled) particles. Typically, after one metastable phase nucleates, the rapid release of the heat of fusion causes droplet recalescence and this can allow the nucleation of another metastable phase at a somewhat higher temperature [34–36]. This phenomenon is revealed by the microstructure shown Fig. 6 (a cross section of a particle from the <20 μm size range) where it would appear that α-Fe nucleated at a deep undercooling but its growth into the liquid was terminated by the nucleation and growth of the silicide phase from another location in the droplet. However, micron-sized Nb(C,N) particles are still evident in the microstructure suggesting that the cooling rate was not sufficiently rapid to suppress the formation of this stable phase. The detailed microstructure in a particle such as this is shown in the TEM images of Figs. 7 and 8 where it can also be seen that fine scale Nb(C,N) particles also form. Primary angular Nb(C,N) particles appear to have been engulfed by the silicide phase whilst much finer 20 to 50 nm sized secondary Nb(C,N) particles are seen (Fig. 8) in the last to solidify cell boundaries. The silicide phase (Table 4) is close in composition to that reported by Bowden [5].

One further point to note is the existence of silicide crystal structures with two distinct lattice parameters (Fig. 2) and the reasons for this are not fully understood at present. One possible explanation is that powder particles with different solidification pathways are present in a given powder size fraction. Therefore, it is possible that some powder particles will follow the solidification path revealed by Fig. 6 (independent nucleation from the melt of a silicide grain), whereas in other particles a grain of primary α-Fe or γ-Fe could nucleate first with silicide phase forming interdendritically as opposed to nucleating directly from the melt. The compositions of the silicide phases are evidently different from the stoichiometric values of the equilibrium structures and this is most probably due to the fact that they formed under highly non-equilibrium conditions. The compositions measured here are close to those reported by Bowden et al. in their work on a multicomponent alloy related to the one studied here [5].

In the gas atomisation process a liquid metal stream is broken up into droplets by impinging gas jets [18]. The gas stream is turbulent, and this causes a stochastic dispersion of liquid droplets of different sizes to form. However, the cooling rate of a given size of droplet will depend not only on its diameter. The cooling rate will also be affected by the trajectory a droplet follows in the turbulent gas stream. The consequence of this is that, even in powder particles of similar diameters, different microstructures can be expected. XRD patterns, which arise from the collection of diffracted X-rays from large numbers of individual particles, obviously capture this stochastic variability in phase selection and represent average characteristics of a powder size fraction. In contrast, microscopy permits imaging of only limited numbers of individual particles and, indeed, planar sections through them.

Overall, it is evident that in this complex alloy system, metastable phases can form in small diameter particles as a result of the high cooling rates to which they are subject. In the manufacture of critical components from HIP consolidated powder it is potentially important to avoid microstructural variability in the powder. The current study demonstrates, therefore, that the classification of atomised powder

should be considered prior to HIPing in an effort to avoid the inclusion of particles containing the non-equilibrium microstructures that may degrade the performance of HIPed components.

5. Conclusions

1. Gas atomised powders of Tristelle 5183 (Fe-21%Cr-10%Ni-7%Nb-5% Si-2%C in wt%) exhibit phase proportions which change with powder particle size range i.e. cooling rate. Estimates of the cooling rate of liquid droplets indicate a change from approximately 8×10^4 to 7×10^5 K/s for droplet sizes of 75 and 20 μm respectively.
2. Particles of diameter greater than approximately 53 μm contain dendritic fcc γ-Fe as the principal phase with smaller quantities of α-Fe, an interdendritic silicide phase isostructural to $Fe_5Ni_3Si_2$ and ~5% Nb (C,N). Particles <53 μm have increasing quantities of either dendritic α-Fe or cellular silicide phase with decreasing amounts of γ-Fe as the particle size decreases, along with ~5% Nb(C,N).
3. Coarse (>10 μm) sized Nb(C,N) particles, seen in all powder size fractions, pre-existed in the melt prior to atomisation, whereas micron-sized Nb(C,N) that are found within α-Fe, γ-Fe or silicide are the primary solidification phase. Nanoscale Nb(C,N) also formed interdendritically, or in the cell boundaries of the silicide phase, in the last stages of solidification.
4. The Nb(C,N) XRD reflections from the gas atomised powders have been deconvoluted into three populations related to the three distinct Nb(C,N) morphologies. It is argued that one set of crystals consistent with the Nb(C,N) phase formed under near-equilibrium conditions whereas the other two populations formed under non-equilibrium conditions and appear to be carbon deficient with respect to stoichiometric Nb(C,N).
5. The increasing quantities of α-Fe and silicide in smaller sized powder particles is consistent with increased undercooling prior to nucleation permitting metastable phase formation.
6. Rapid solidification processing significantly alters the solidification pathway of this alloy with the complete disappearance of an M_7C_3 phase which is found in significant quantities in a conventional mould cast sample which forms NbC, γ-Fe, M_7C_3, α-Fe and silicide phase in the as-cast condition.

Data availability

The raw/processed data required to reproduce these findings cannot be shared at this time due to legal or ethical reasons.

Acknowledgements

The authors gratefully acknowledge funding from Rolls-Royce plc. M.J. Carrington also acknowledges funding from the Faculty of Engineering, University of Nottingham in support of a PhD studentship. The authors thank the Nanoscale and Microscale Research Centre (nmRC) for providing access to instrumentation and Dr. Michael W. Fay for technical assistance. Access to the JEOL 7100F FEG-SEM was supported by the Engineering and Physical Sciences Research Council (EPSRC) [grant number EP/L022494/1] and the University of Nottingham. The authors also wish to thank Dr. Geoff West of the Warwick Manufacturing Group (WMG) at the University of Warwick for his technical assistance concerning TEM and TEM sample preparation.

Appendix A. Supplementary data

Supplementary data to this article can be found online at https://doi.org/10.1016/j.matdes.2018.107548.

References

[1] M. Riddihough, Stellite as a wear-resistant material, Tribology 3 (1970) 211–215, https://doi.org/10.1016/0041-2678(70)90058-8.
[2] T. Nazarewicz, Cobalt: a critical commodity, Resource World 2016, pp. 52–53.
[3] P. Aubry, Survey on Stellite Substitutes for hardfacing in nuclear environments, https://www.eera-jpnm.eu/filesharer/documents/_Euratom_Projects/Pastprojects/MATTERpublicdeliverables/DeliverableD7.2MATTER.pdf 2012.
[4] S. Atamert, J. Stekly, Microstructure, wear resistance, and stability of cobalt based and alternative iron based hardfacing alloys, Surf. Eng. 9 (1993) 231–240, https://doi.org/10.1179/sur.1993.9.3.231.
[5] D. Bowden, Y. Krysiak, L. Palatinus, D. Tsivoulas, S. Plana-Ruiz, E. Sarakinou, U. Kolb, D. Stewart, M. Preuss, A high-strength silicide phase in a stainless steel alloy designed for wear-resistant applications, Nat. Commun. 9 (2018) 1–10, https://doi.org/10.1038/s41467-018-03875-9.
[6] D. Bowden, D. Stewart, M. Preuss, Understanding the microstructural evolution of silicide-strengthened hardfacing steels, Mater. Des. 161 (2019) 1–13, https://doi.org/10.1016/j.matdes.2018.09.015.
[7] V.L. Ratia, D. Zhang, M.J. Carrington, J.L. Daure, D.G. McCartney, P.H. Shipway, D.A. Stewart, The effect of temperature on sliding wear of self-mated HIPed Stellite 6 in a simulated PWR environment, Wear (2018)https://doi.org/10.1016/j.wear.2018.09.012 In press.
[8] B. Barzdajn, A.T. Paxton, D. Stewart, F.P.E. Dunne, A crystal plasticity assessment of normally-loaded sliding contact in rough surfaces and galling, J. Mech. Phys. Solids 121 (2018) 517–542, https://doi.org/10.1016/j.jmps.2018.08.004.
[9] J.K. Kim, S.J. Kim, The temperature dependence of the wear resistance of iron-base NOREM 02 hardfacing alloy, Wear 237 (2000) 217–222, https://doi.org/10.1016/S0043-1648(99)00326-9.
[10] Anon, News & Views, Powder Metall. 36 (1993) 77–97, https://doi.org/10.1179/pom.1993.36.2.77.
[11] R.T. Smith, J.A. Siefert, D. Gandy, S.S. Babu, Tribolayer formation by strain-induced transformations in hardfacing alloys, in: D. Gandy, J. Shingledecker (Eds.), Adv. Mater. Technol. Foss. Power Plants, ASM International, Materials Park, OH 2014, pp. 482–490.
[12] P. Crook, R.D. Zordan, Nuclear Grade Steels, US Patent Num: 4,643,767, 1987.
[13] C. Zhao, D. Stewart, J. Jiang, F.P.E. Dunne, A comparative assessment of iron and cobalt-based hard-facing alloy deformation using HR-EBSD and HR-DIC, Acta Mater. 159 (2018) 173–186, https://doi.org/10.1016/j.actamat.2018.08.021.
[14] R. Smith, M. Doran, D. Gandy, S. Babu, L. Wu, A.J. Ramirez, P.M. Anderson, Development of a gall-resistant stainless-steel hardfacing alloy, Mater. Des. 143 (2018) 38–48, https://doi.org/10.1016/j.matdes.2018.01.020.
[15] R.T. Smith, T. Lolla, D. Gandy, L. Wu, G. Faria, A.J. Ramirez, S.S. Babu, P.M. Anderson, In situ X-ray diffraction analysis of strain-induced transformations in Fe- and Co-base hardfacing alloys, Scr. Mater. 98 (2015) 60–63, https://doi.org/10.1016/j.scriptamat.2014.11.003.
[16] B.V. Cockeram, Corrosion resistance and electrochemical potentiokinetic reactivation testing of some iron-based hardfacing alloys, Corrosion 56 (2000) 849–859, https://doi.org/10.5006/1.3280588.
[17] H.V. Atkinson, B.A. Rickinson, Hot Isostatic Processing, Springer, London, 1991.
[18] A.J. Yule, J.J. Dunkley, Atomization of Melts for Powder Production and Spray Deposition, Oxford University Press, Oxford, 1994.
[19] J.L. Sulley, I. Hookham, B. Burdett, K. Bridger, R. Uk, Introductuion of Hot Isostatically Pressee, Reactor Coolant System Components in PWR Plant, Proc. 18th Int. Conf. Nucl. EngVol. 1, American Society of Mechanical Engineers, Xi'an 2010, pp. 357–367, https://doi.org/10.1115/ICONE18-30253.
[20] D. Stewart, J.L. Sulley, Hiped hard facings for nuclear applications - materials, key potential defects and mitigating quality control measures, Proc. 2016 24th Int. Conf. Nucl. EngAmerican Society of Mechanical Engineers, Charlotte, 2016https://doi.org/10.1115/ICONE24-61106 , (Paper N.ICONE24-61106).
[21] E.K.H. Li, P.D. Funkenbusch, Hot isostatic pressing (HIP) of powder mixtures and composites: packing, densification, and microstructural effects, Metall. Trans. A. 24 (1993) 1345–1354, https://doi.org/10.1007/BF02668202.
[22] K. Li, Microstructure evolution of gas-atomized Fe – 6.5 wt% Si droplets, J. Mater. Res. 29 (2014) 527–534, https://doi.org/10.1557/jmr.2014.12.
[23] B. Zheng, Y. Lin, Y. Zhou, E.J. Lavernia, Gas atomization of amorphous aluminum powder: part II. Experimental investigation, Metall. Mater. Trans. B Process Metall. Mater. Process. Sci. 40 (2009) 995–1004, https://doi.org/10.1007/s11663-009-9277-4.
[24] A.M. Mullis, L. Farrell, R.F. Cochrane, N.J. Adkins, Estimation of cooling rates during close-coupled gas atomization using secondary dendrite arm spacing measurement, Metall. Mater. Trans. B Process Metall. Mater. Process. Sci. 44 (2013) 992–999, https://doi.org/10.1007/s11663-013-9856-2.
[25] P.A.P. Perez, J.L. Gonzalez-Carrasco, Influence of the powder particle size on tensile properties of Ni3A1 processed by rapid solidification and hot isostatic pressing, Mater. Sci. Eng. 199 (1995) 211–218.
[26] R.A. Young, The Rietveld Method, Oxford University Press, Oxford, 1995.
[27] R.W. Cheary, A. Coelho, Fundamental parameters approach to X-ray line-profile fitting, J. Appl. Crystallogr. 25 (1992) 109–121, https://doi.org/10.1107/S0021889891010804.
[28] N. Krendelsberger, F. Weitzer, Y. Du, J.C. Schuster, Constitution of the ternary system Cr-Ni-Ti, J. Alloys Compd. 575 (2013) 48–53, https://doi.org/10.1016/j.jallcom.2013.04.061.
[29] S. Ackerbauer, N. Krendelsberger, F. Weitzer, K. Hiebl, J.C. Schuster, The constitution of the ternary system Fe–Ni–Si, Intermetallics 17 (2009) 414–420, https://doi.org/10.1016/j.intermet.2008.11.016.

[30] E.I. Gladyshevskii, P.I. Kripyakevich, Y.B. Kuz'ma, The crystal structure of low-silicon ternary compounds in the Cr-Ni-Si and Cr-Co-Si systems, J. Struct. Chem. 3 (1962) 402–410, https://doi.org/10.1007/BF00744082.
[31] J.A. Dantzig, M. Rappaz, Solidification, 2nd edition EPFL Press, 2016.
[32] J.O. Anderson, T. Helander, L. Höglund, P. Shi, B. Sundman, Thermo-Calc and DICTRA, Computational tools for materials science, Calphad. 26 (2002) 273–312, https://doi.org/10.1016/S0364-5916(02)00037-8.
[33] E.K. Storms, N.H. Krikorian, The variation of lattice parameter with carbon content of niobium carbide, J. Phys. Chem. 63 (1959) 1747–1749, https://doi.org/10.1021/j150580a042.
[34] D. Herlach, P. Galenko, D. Holland-Mortiz, Metastable Solids From Undercooled Melts, 1st ed. Elsevier, 2007.
[35] G. Shao, P. Tsakiropoulos, Prediction of phase selection in rapid solidification using time dependent nucleation theory, Acta Metall. Mater. 42 (1994) 2937–2942, https://doi.org/10.1016/0956-7151(94)90391-3.
[36] J.H. Perepezko, Nucleation-controlled reactions and metastable structures, Prog. Mater. Sci. 49 (2004) 263–284, https://doi.org/10.1016/S0079-6425(03)00028-8.
[37] A. Zambon, B. Badan, A.F. Norman, Development of Solidification Microstructures in Atomized Fe-Ni Alloy Droplets, 225, 1997 119–123.
[38] T.F. Kelly, M. Cohen, J.B. Vander Sande, Rapid solidification of a droplet-processed stainless steel, Metall. Trans. A. 15 (1984) 819–833, https://doi.org/10.1007/BF02644556.